

Quantum Phases of Transition Metal Dichalcogenide Moiré Systems

Yiqing Zhou¹, D. N. Sheng², and Eun-Ah Kim¹

¹Laboratory of Atomic and Solid State Physics, Cornell University, Ithaca, New York 14853, USA

²Department of Physics and Astronomy, California State University, Northridge, California 91330, USA

 (Received 18 June 2021; accepted 29 March 2022; published 14 April 2022)

Moiré systems provide a rich platform for studies of strong correlation physics. Recent experiments on heterobilayer transition metal dichalcogenide Moiré systems are exciting in that they manifest a relatively simple model system of an extended Hubbard model on a triangular lattice. Inspired by the prospect of the hetero-transition metal dichalcogenide Moiré system's potential as a solid-state-based quantum simulator, we explore the extended Hubbard model on the triangular lattice using the density matrix renormalization group. Specifically, we explore the two-dimensional phase space spanned by the key tuning parameters in the extended Hubbard model, namely, the kinetic energy strength and the further-range Coulomb interaction strengths. We find competition between Fermi fluid, chiral spin liquid, spin density wave, and charge order. In particular, our finding of the optimal further-range interaction for the chiral correlation presents a tantalizing possibility.

DOI: 10.1103/PhysRevLett.128.157602

The triangular lattice Hubbard model has long been of intense interest [1–14], since the geometric frustration and quantum fluctuation can lead to a rich set of possibilities. In particular, previous density matrix renormalization group (DMRG) studies have shown a robust metal-insulator transition (MIT) at half-filling [4]. More recently, the possibility of the chiral spin liquid (CSL) phase pre-empting the MIT [7,12] has been predicted. Other possible ordered phases have been proposed [13]. However, the well-studied standard Hubbard model dismisses the long-range interactions which are ubiquitous in materials explored in experiments; therefore, predictions made by previous works are challenging to test in realistic experimental setups.

Following the proposal of [15] that heterobilayer transition metal dichalcogenide (TMD) moiré systems can realize the triangular lattice Hubbard model [16], recent experiments on hetero-TMD moiré systems have indeed observed Mott insulating states at half-filling [17,18]. Furthermore, continuous control over hopping strength relative to the interaction strength is now accessible [19,20]. However, as evidenced by the charge order at fractional fillings [21,22] the TMD systems have further-range interactions due to a low charge density and resulting low screening. Excitingly, these further-range interactions can also be tuned in experiments [19], presenting a two-dimensional space, spanned by the hopping and the further range interaction strengths with respect to the on-site Coulomb interaction strength, to explore a plethora of quantum phases. In comparison, computational investigations have so far been restricted to systems with only on-site interactions, confining us to a one-dimensional phase space controlled purely by the ratio of on-site Coulomb interaction and hopping strength.

Motivated by the experimental developments, in this Letter, we explore the extended Hubbard model on a triangular lattice and study the phase space upon tuning the ratio of hopping to on-site interaction t/U and the relative strengths of long-range interactions parametrized by V_1/U [Fig. 1(b)]. Using DMRG, we make the first pass over this large phase space and benchmark our results against the standard Hubbard model limit [4,5,7,12]. By studying the effect of further-range interactions, we study competition between charge order, chiral spin liquid, and spin density wave at half-filling. The rest of the Letter is organized as follows. We first introduce the extended Hubbard model under study and identify a rich phase diagram with Fermi fluid (FF), CSL, and spin density wave (SDW) phases in a weak long-range interaction region, showing consistency between the extended Hubbard model in the small V_1/U limit and the standard Hubbard model. Interestingly, we find that intermediate long-range interaction can enhance the chiral order. Finally, we discuss the charge-ordered states (CO) promoted by stronger long-range interactions. We close with a summary of the quantum phases we observe and provide future outlooks.

Model.—We consider the following extended Hubbard model on a triangular lattice,

$$H = -t \sum_{\langle ij \rangle} (c_i^\dagger c_j + \text{H.c.}) + U \sum_i n_{i,\uparrow} n_{i,\downarrow} + V_1 \sum_{\langle ij \rangle} n_i n_j + V_2 \sum_{\langle\langle ij \rangle\rangle} n_i n_j + V_3 \sum_{\langle\langle\langle ij \rangle\rangle\rangle} n_i n_j, \quad (1)$$

where t, U, V_i represent hopping, on-site interaction, i th nearest neighbor interaction strength, respectively.

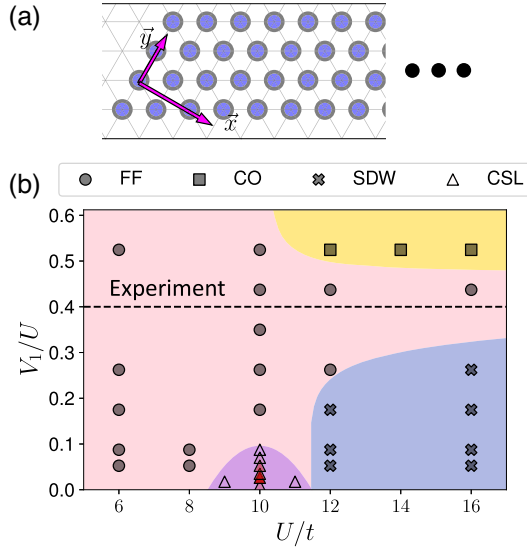


FIG. 1. The system under study and the phase diagram. (a) A partial sketch of a YC4 cylinder used in the DMRG calculation, where x, y directions are specified by the arrows. The number of lattice sites along the y direction $L_y = 4$. The boundary condition is periodic in y and open along the cylinder axis direction. (b) The phase diagram of the extended Hubbard model on a triangular lattice. The symbols represent phases observed using DMRG; the color shadings are the schematic extents of the phases. The color intensity of the CSL markers (triangles) represents the strength of chiral ordering. The dashed line marks the V_1/U accessed by an instance of the experimental setup.

We follow a heterobilayer TMD experiment setup [19] and set $V_2/V_1 \approx 0.357$ and $V_3/V_1 \approx 0.260$ (derivation shown in Supplemental Material [23]). The choice of V_2/V_1 and V_3/V_1 does not quantitatively change the phases observed in the phase space within an experimentally feasible parameter range (see Supplemental Material [23] for results comparing different V_2/V_1 and V_3/V_1 ratios). Therefore, the relative strength of further-range interactions is tuned by the single parameter V_1/U . Given the independent experimental control over the bandwidth and the range of interaction, we explore the ground state in a phase space spanned by the on-site interaction strength U/t and the further-range interaction strength represented by V_1/U . With the MIT in mind, we focus on the half-filling state at zero total spin $S = 0$. We perform large-scale DMRG calculations on YC4 cylinders as sketched in Fig. 1(a). Note that the YC n (XC n) cylinders have one of the lattice edge parallel (perpendicular) to the periodic direction and have n sites ($n/2$ unit cells) along the periodic direction. To investigate the effect of further-range interaction on the CSL phase, we focus on YC geometry in which previous studies on standard triangular Hubbard model have observed that chiral phase is easier to observe [7,12] as opposed to the XC geometry. The YC4 geometry can lead to double counting in the second and third nearest neighboring sites; we avoid the double counting by coupling

each pair of sites only once. We compare various cylinder lengths, $L_x = 16, 32, 48$, and keep 10000 to 30000 [24] states to get high-accuracy numerical results (see Supplemental Material [23] for more details).

We observe a rich phase space in a parameter space reachable by existing experimental devices. As shown in Fig. 1(b), the phases we observe include CSL, SDW, CO, and FF, with the long-range interactions further enriching the phase space compared to the standard Hubbard model. In the absence of further-range interactions, the system in the large U/t limit can be well-captured by an effective spin model [25] with antiferromagnetic nearest neighbor interaction driven by superexchange on the triangular lattice. The quantum fluctuation in intermediate U/t with the geometric frustration of the triangular lattice might drive CSL [26]. The further-range interaction V_1 can impact the ground state both in the spin and charge sectors. First, in the small V_1/U limit, V_1 interaction enhances the spin exchange interactions by a factor $U/(U - V_1)$, while it can also be mapped to ferromagnetic direct exchange interaction between nearest neighbors, suppressing antiferromagnetic ordering tendencies. This expectation is borne out in our discovery that the chiral order peaks at a finite small V_1/U in the intermediate U/t range as highlighted by the color intensity in Fig. 1(b). Second, as the long-range interaction strength increases, charge order is promoted, and spin ordering is suppressed. Thus we see the melting of CSL and SDW and then the emergence of CO as V_1/U increases [27]. The richness of the phase space demonstrates the importance of long-range interactions. Beyond the intuitive understanding of these phases, we present detailed numerical evidence for each phase below.

Small V_1/U limit.—In the small V_1/U limit ($V_1/U \approx 0.0175$), we reproduce the latest results of the Hubbard model with $V_1/U = 0$ [5,7,12]. First, we detect the MIT by calculating the double occupancy, $n_d = \langle n_\uparrow n_\downarrow \rangle$. It shows a discontinuous drop at the critical value of $(U/t)_{\text{MIT}} \sim 9.2$, upon increasing U/t [Fig. 2(a)]. This observation is consistent with an earlier study [12], which reports the MIT at $U/t \approx 9.0$ for the Hubbard model.

Next, we identify the above metal-insulator transition to take the system into a CSL phase by calculating the spin structure factor [Fig. 2(c)] and the chiral correlation function (Fig. 3). We consider the chiral correlation function $\langle \chi_m \chi_n \rangle$, where the chiral order parameter $\chi_i = \vec{S}_i \cdot (\vec{S}_j \times \vec{S}_k)$ is defined on a triangle centered around lattice site i , involving all three corner sites i, j , and k [28]. We observe, in Fig. 2(b) between $U/t \approx 9.4$ and 10.8, a long-range chiral correlation $\langle \chi_i \chi_j \rangle$ that is orders of magnitude higher than that in neighboring phases. The lower boundary of the long-range chiral correlation $U/t \approx 9.4$ matches where the MIT is observed from the double occupancy [see Fig. 2(a)]. In addition, the featureless spin structure factor $\langle S_q(\vec{k}) \rangle = (1/N) \sum_{ij} e^{i\vec{k} \cdot \vec{r}_{ij}} \langle \vec{S}_i \cdot \vec{S}_j \rangle$

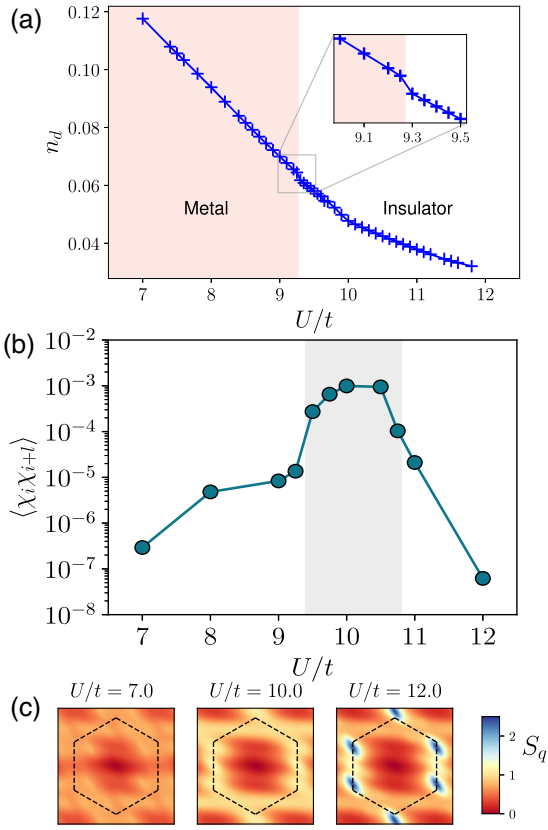


FIG. 2. Small V_1/U limit. (a) Double occupancy n_d as a function of U/t at $V_1/U \approx 0.0175$. The discontinuous drop highlighted in the inset shows the transition from a metallic to an insulating phase. Data are from 4×16 YC cylinder calculations. (b) Chiral correlation function $\langle \chi_i \chi_{i+l} \rangle$ versus U/t at $V_1/U \approx 0.0175$ in a log scale. As a guide to the eye, the gray shaded region marks the range of U/t where CSL lives. (c) Spin structure factors $\langle S_q(\vec{k}) \rangle$ plotted in momentum space at $V_1/U \approx 0.0175$. Three panels correspond to $U/t = 7.0$, 10.0 , and 12.0 from left to right, respectively. The black dashed lines mark the boundary of the Brillouin zone. Data are from 4×32 YC cylinders for (b),(c).

confirms the absence of magnetic order associated with the intermediate U/t insulating phase. Note that the slight anisotropy is caused by the finite-size geometry of the YC4 cylinders. We also analyze the real space correlation function in Supplemental Material [23]. Observing long-range chiral correlations that are at the same order of magnitude as reported in Refs. [7,12] for the Hubbard model with $V = 0$ [29], we conclude that the insulating state immediately after the MIT is CSL.

Increasing U/t further, we observe an additional phase transition within the insulating phase. Upon this second transition, the spin structure factor gains sharp peaks at corners of the Brillouin zone [see Fig. 2(c)]. Similar peaks in $\langle S_q(\vec{k}) \rangle$ have been observed in the Hubbard model [5,12]. These peaks distinguish the large U/t insulating

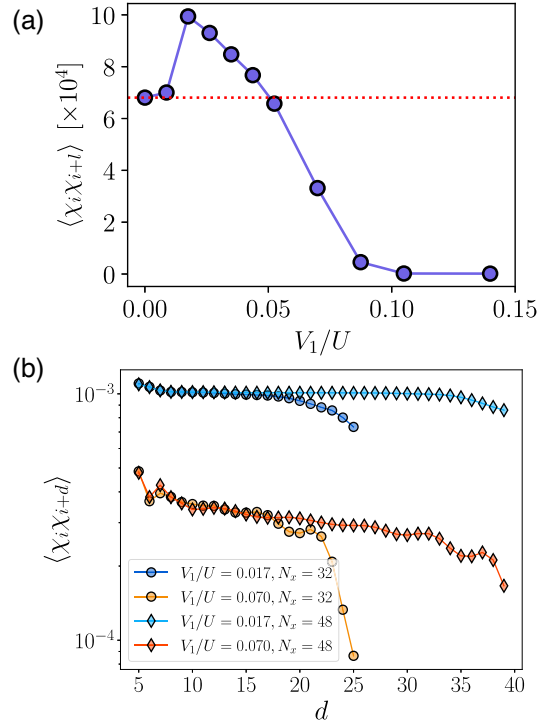


FIG. 3. Chiral correlation function. (a) Chiral correlation function $\langle \chi_i \chi_{i+l} \rangle$ versus V_1/U at $U/t = 10.0$. The red dashed horizontal line denotes $\langle \chi_i \chi_{i+l} \rangle$ at $V_1/U = 0$. Data points are obtained from 4×32 cylinders, and the site separation is chosen to be by half the cylinder length, $l = L_x/2 = 16$. (b) Chiral correlation $\langle \chi_i \chi_{i+d} \rangle$ as a function of site separation d with fixed $U/t = 10.0$ and different V_1/U . Results from two systems sizes, $L_y = 4$, $L_x = 32$, and 48 are presented.

phase from the intermediate U/t CSL phase and show evidence of the emergence of spin density waves with wave vectors $\mathbf{Q}_{\text{SDW}} = (\sqrt{3}\pi/2a, \pi/2a)$ and $(\sqrt{3}\pi/2a, -\pi/2a)$. At the same time, the chiral correlation dives down, indicating the nonchiral nature of the spin density wave state [see Fig. 2(b)].

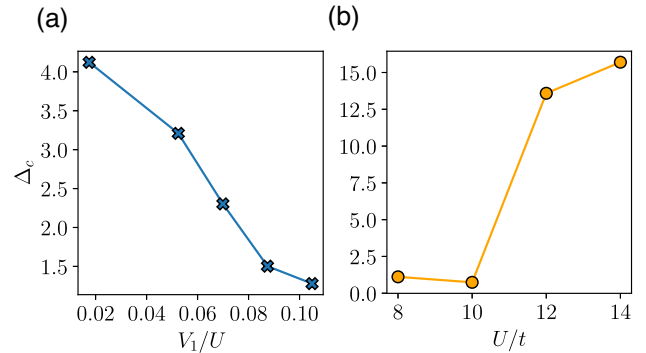


FIG. 4. Charge gap. (a) Charge gap Δ_c along a vertical cut in phase diagram at $U = 10$ with varying further-range interaction strength parametrized by V_1/U . (b) Charge gap along a horizontal cut in phase diagram at $V_1/U \approx 0.6119$ with varying U/t .

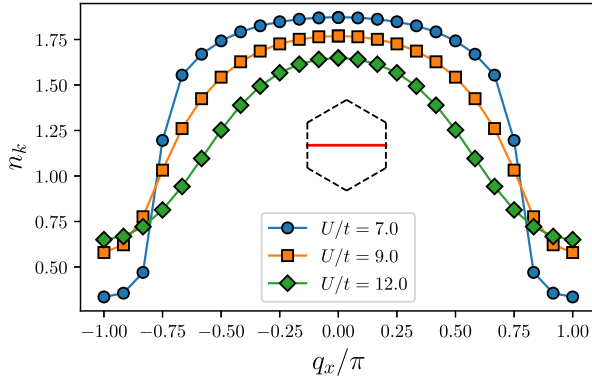


FIG. 5. Electron momentum distribution n_k along a momentum space cut at fixed further-range interaction strength $V_1/U = 0.0175$ and various on-site interaction strengths $U/t = 7.0$, 9.0 , and 12.0 . The inset shows a Brillouin zone with the cut marked by the red line.

Effects of further-range interactions.—We study phase transitions driven by the further-range interactions, fixing the on-site interaction strength at $U/t = 10$, which is close to the center of the CSL phase. The further-range interaction has a nonmonotonic effect on the CSL phase as it is shown through the chiral correlation at half the length of the YC4 cylinder, $l = L_x/2$ as a function of V_1/U in Fig. 3(a). The nonmonotonicity comes with the dramatic enhancement in the chiral correlation at intermediate V_1/U compared to the original Hubbard model. Upon further increasing V_1/U , the system leaves the sweet spot, and chiral correlation dies out at $V_1/U \gtrsim 0.07$. Within the CSL phase, we investigate the chiral correlation strength as a function of distance d . As shown in Fig. 3(b), we find the chiral correlation to be long ranged, nearly constant as a function of d in the CSL phase. We present results from systems with $L_x = 32$ and 48 . Despite the finite-size effects near the end of the cylinder, both systems have consistent

chiral correlation strength. The region of nearly constant correlations grows with L_x , indicating true chiral order at the large L_x limit.

As V_1/U increases, the CSL melts into a Fermi fluid phase. As shown in Fig. 4, we look at the charge gap Δ_c along a vertical line in the phase diagram (Fig. 1) at $U/t = 10$. The charge gap diminishes as the further-range interaction strength increases, showing evidence of the melting of CSL insulating phase to a FF phase. This FF phase fills in the large space between CSL, SDW, and CO in the phase diagram. The FF being a gapless phase makes it challenging to investigate in a finite size study, and thus we hereby focus mainly on the qualitative signature of FF.

The signature of this phase lies in its electron momentum distribution $n_k = (1/N) \sum_{ij} e^{-ik \cdot \vec{r}_{ij}} \langle c_i^\dagger c_j \rangle$. The representative data for FF are obtained at $V_1/U \approx 0.0175$ as shown in Fig. 5. At $U/t = 7.0$, which is in the FF phase, we observe a rapid drop in occupation at $q_x/\pi = 0.75$, resembling a finite residue similar to a Fermi liquid (for larger $U/t \gtrsim 12$ in FF, the nature of the liquid phase becomes more complex and difficult to be characterized, which we leave for future studies). In contrast, other phases show continuous changes in n_k through the Brillouin zone.

In the large U/t region, increasing further-range interactions parametrized by V_1/U melts the SDW into FF and then drives the formation of CO. Figure 6(a) shows the spin structure factor $\langle S_q(\vec{k}) \rangle$ along a cut in the momentum space. We observe that the amplitude of the $\langle S_q(\vec{k}) \rangle$ peaks decreases as V_1/U increases, and ultimately the peaks disappear at $V_1/U \approx 0.2$. Increasing the further-range interaction strength across $V_1/U \approx 0.2$, we see the FF until the CO emerges at $V_1/U \approx 0.5$. We identify the existence of CO from the charge density with a shift to remove amplitude at zero wave vector, $N_k = (1/\sqrt{N}) \sum_i (n_i - 1) e^{-ik \cdot \vec{r}_i}$. As shown in Fig. 6(b), peaks in N_k appear at two corners of the Brillouin zone, corresponding to CO wave vector

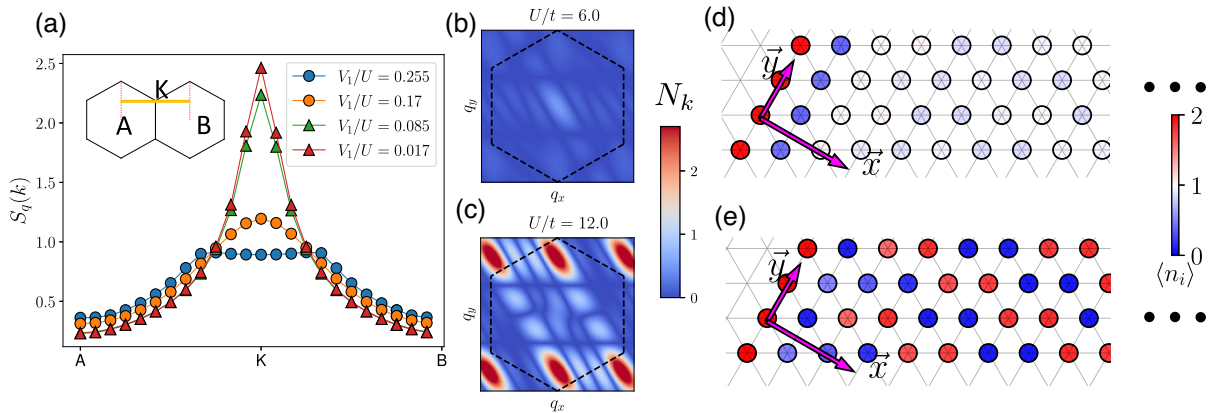


FIG. 6. Large U/t limit. (a) Spin structure factor $S_q(k)$ with $U/t = 12.0$ at various V_1/U along a cut in momentum space highlighted by the yellow line in the inset. The peaks are observed around the K point. Panels (b)–(e) show charge density at $V_1/U \approx 0.612$. (b) Charge density in momentum space N_k for $U/t = 6.0$. (c) N_k for $U/t = 12.0$. The black dashed lines represent the boundary of the Brillouin zone. (d) Charge density in real space n_i for $U/t = 6.0$. (e) n_i for $U/t = 12.0$.

$\mathbf{Q}_{\text{CO}} = (0, \pi/a)$, where a is the lattice constant. Alternatively, in Fig. 6(c), we show the charge density in real space. Given the circular Fermi surface (see Supplemental Material [23], Appendix E) and wave vector far from $2k_F$, the CO is not driven by nesting or the quasi 1D geometry. Rather, as the strong coupling analysis in Appendix E suggests the observed CO is driven by strong coupling physics, as in the generalized Wigner crystal phenomena so far only observed at fractional filling [17,21,30].

Conclusion and outlook.—In summary, we investigated the triangular lattice Hubbard model with an extended range of interactions, as motivated by recent experimental developments in hetero-TMD moiré systems. Specifically, we explored the two-dimensional phase diagram controlled by the electron hopping t and the further-range interactions V_1 . In the small V_1/U limit, we reproduce results from [5,7,12] showing transitions from a metallic state to a chiral spin liquid and then to a spin density wave phase as U/t increases. Upon increasing long-range interactions V_1 , V_2 , and V_3 , we find that the chiral spin liquid is strengthened with small long-range interaction before it gives way to the metallic state. On the other hand, the spin density wave is continuously weakened by increasing long-range interactions. Further increasing further-range interactions, the CO emerges with the wave vector that is not dictated by the quasi-1D geometry of the simulation but rather has periodicity in the direction perpendicular to the cylinder long direction (the x direction as shown in Fig. 6).

The enhancement of chiral correlation with small but finite further-range interaction we observed presents a tantalizing potential. While we cannot rule out the finite size effect, one possible mechanism for such a phenomena would be that further-range interaction-driven direct exchange can suppress SDW ordering and further frustration. The observation warrants further computational and experimental exploration. The MIT between the interaction-driven CO state and the FF has the potential of supporting a superconducting state that preempts the MIT, similar to the CSL phase preempting the direct phase transition between FF and SDW. Given that the CO state has a localized doubly occupied site, introducing phase coherence and liberating the pairs to move could result in a pair density wave state [14] in an experimentally realizable setting. Our preliminary results support such a possibility, which is an interesting direction for future investigation [31]. In general, the rich phase diagram we uncovered upon tuning the further-range interactions can guide experimental exploration of the new solid-state quantum simulator platform of hetero-TMD moiré systems.

The authors thank Kin Fai Mak and Jie Shan for helpful discussions. Part of the DMRG calculation uses the ITensor package [32]. DMRG simulations at Cornell were carried out on the Red Cloud at the Cornell University Center for Advanced Computing, with the support of the DOE under

Award No. DE-SC0018946. E. A. K. and Y. Z. acknowledge support by the National Science Foundation through Award No. OAC-1934714 (Institutes for Data-Intensive Research in Science and Engineering Frameworks), and through the NSF MRSEC program (No. DMR-1719875) for the initial design of the studies. Y. Z. and E. A. K. acknowledge support from the Cornell College of Arts and Sciences through the New Frontier Grant. This research is funded in part by the Gordon and Betty Moore Foundation through Grant No. GBMF10436 to E. A. K. to support the work of Y. Z. D. N. S. acknowledges the support by the U.S. Department of Energy, Office of Basic Energy Sciences, under Grant No. DE-FG02-06ER46305.

-
- [1] P. Sahebsara and D. Sénéchal, *Phys. Rev. Lett.* **100**, 136402 (2008).
 - [2] T. Yoshioka, A. Koga, and N. Kawakami, *Phys. Rev. Lett.* **103**, 036401 (2009).
 - [3] H.-Y. Yang, A. M. Läuchli, F. Mila, and K. P. Schmidt, *Phys. Rev. Lett.* **105**, 267204 (2010).
 - [4] R. V. Mishmash, I. González, R. G. Melko, O. I. Motrunich, and M. P. A. Fisher, *Phys. Rev. B* **91**, 235140 (2015).
 - [5] T. Shirakawa, T. Tohyama, J. Kokalj, S. Sota, and S. Yunoki, *Phys. Rev. B* **96**, 205130 (2017).
 - [6] J. Venderley and E.-A. Kim, *Phys. Rev. B* **100**, 060506(R) (2019).
 - [7] A. Szasz, J. Motruk, M. P. Zaletel, and J. E. Moore, *Phys. Rev. X* **10**, 021042 (2020).
 - [8] Z. Zhu, D. N. Sheng, and A. Vishwanath, *arXiv:2007.11963*.
 - [9] X.-Y. Song, A. Vishwanath, and Y.-H. Zhang, *Phys. Rev. B* **103**, 165138 (2021).
 - [10] Y. Gannot, Y.-F. Jiang, and S. A. Kivelson, *Phys. Rev. B* **102**, 115136 (2020).
 - [11] A. Szasz and J. Motruk, *Phys. Rev. B* **103**, 235132 (2021).
 - [12] B.-B. Chen, Z. Chen, S.-S. Gong, D. N. Sheng, W. Li, and A. Weichselbaum, *arXiv:2102.05560*.
 - [13] A. Wietek, R. Rossi, F. Šimkovic IV, M. Klett, P. Hansmann, M. Ferrero, E. M. Stoudenmire, T. Schäfer, and A. Georges, *Phys. Rev. X* **11**, 041013 (2021).
 - [14] C. Peng, Y.-F. Jiang, Y. Wang, and H.-C. Jiang, *New J. Phys.* **23**, 123004 (2021).
 - [15] F. Wu, T. Lovorn, E. Tutuc, and A. H. MacDonald, *Phys. Rev. Lett.* **121**, 026402 (2018).
 - [16] D. M. Kennes, M. Claassen, L. Xian, A. Georges, A. J. Millis, J. Hone, C. R. Dean, D. N. Basov, A. N. Pasupathy, and A. Rubio, *Nat. Phys.* **17**, 155 (2021).
 - [17] E. C. Regan, D. Wang, C. Jin, M. I. B. Utama, B. Gao, X. Wei, S. Zhao, W. Zhao, Z. Zhang, K. Yumigeta *et al.*, *Nature (London)* **579**, 359 (2020).
 - [18] Y. Tang, L. Li, T. Li, Y. Xu, S. Liu, K. Barmak, K. Watanabe, T. Taniguchi, A. H. MacDonald, J. Shan, and K. Fai Mak, *Nature (London)* **579**, 353 (2020).
 - [19] T. Li, S. Jiang, L. Li, Y. Zhang, K. Kang, J. Zhu, K. Watanabe, T. Taniguchi, D. Chowdhury, L. Fu, J. Shan, and K. F. Mak, *Nature (London)* **597**, 350 (2021).
 - [20] A. Ghiotto, E.-M. Shih, G. S. S. G. Pereira, D. A. Rhodes, B. Kim, J. Zang, A. J. Millis, K. Watanabe, T. Taniguchi,

- J. C. Hone, L. Wang, C. R. Dean, and A. N. Pasupathy, *Nature (London)* **597**, 345 (2021).
- [21] Y. Xu, S. Liu, D. A. Rhodes, K. Watanabe, T. Taniguchi, J. Hone, V. Elser, K. F. Mak, and J. Shan, *Nature (London)* **587**, 214 (2020).
- [22] C. Jin, Z. Tao, T. Li, Y. Xu, Y. Tang, J. Zhu, S. Liu, K. Watanabe, T. Taniguchi, J. C. Hone, L. Fu, J. Shan, and K. F. Mak, *Nat. Mater.* **20**, 940 (2021).
- [23] See Supplemental Material at <http://link.aps.org/supplemental/10.1103/PhysRevLett.128.157602> for further details.
- [24] I. P. McCulloch and M. Gulácsi, *Europhys. Lett.* **57**, 852 (2002).
- [25] A. H. MacDonald, S. M. Girvin, and D. Yoshioka, *Phys. Rev. B* **37**, 9753 (1988).
- [26] T. Cookmeyer, J. Motruk, and J. E. Moore, *Phys. Rev. Lett.* **127**, 087201 (2021).
- [27] S. Caprara, M. Avignon, and D. Sarma, *Int. J. Mod. Phys. B* **11**, 2057 (1997).
- [28] We consider the chiral correlation function instead of the chiral order parameter because we use real wave function for the ground state where the $\langle \chi_i \rangle = 0$ due to time-reversal symmetry.
- [29] The chiral order parameter χ in this work is defined in terms of the spin operators, which differs from the definition using Pauli matrices [7] by a factor of 1/8.
- [30] H. Li, S. Li, E. C. Regan, D. Wang, W. Zhao, S. Kahn, K. Yumigeta, M. Blei, T. Taniguchi, K. Watanabe, S. Tongay, A. Zettl, M. F. Crommie, and F. Wang, *Nature (London)* **597**, 650 (2021).
- [31] Y. Zhou, D. N. Sheng, and E.-A. Kim (to be published).
- [32] M. Fishman, S. R. White, and E. M. Stoudenmire, *arXiv*: 2007.14822.